JTTEE5 15:495-500
DOI: 10.1361/105996306X146857
1059-9630/$19.00 © ASM International

Cold Gas Dynamic Spraying of Iron-Base Amorphous Alloy

L. Ajdelsztajn, B. Jodoin, P. Richer, E. Sansoucy, and E.J. Lavernia

(Submitted March 9, 2006; in revised form April 28, 2006)

This paper describes recent efforts to synthesize iron-base amorphous alloys coatings using cold gas dynamic spraying. Characterization of the gas-atomized iron-base (Fe-Cr-Mo-W-C-Mn-Si-Zr-B) powder shows that the powder is fully amorphous when the particle diameter is below 20 μm. The coatings produced were composed of the same microstructure as the one observed in the feedstock powder. The overall deformation suggests the occurrence of a localized deformation process at the particle/particle boundary and a possible adiabatic deformation softening inside the powder particles during splat formation. The synthesis of fully amorphous, porous-free coatings using cold gas dynamic spraying was demonstrated in this work.

Keywords amorphous coatings, cold gas dynamic spraying, nanostructured coatings, nanostructured materials

1. Introduction

Cold gas dynamic spraying, or simply cold spray (CS), is a relatively new high-rate material deposition process. It uses a supersonic gas flow in which fine powder particles are injected and accelerated above a given critical velocity. Upon impact, the solid particles having sufficient kinetic energy deform plastically and bond mechanically to the substrate to form a coating (Ref 1-5). A wide variety of materials have been successfully sprayed such as copper (Cu), conventional and nanocrystalline aluminum (Al) alloys, conventional and nanocrystalline nickel (Ni) alloys, WC-Co, zinc (Zn), and titanium (Ti) to name a few (Ref 1-6). As opposed to other thermal spray processes, CS does not involve any significant heating of the powder particles. Consequently, the process temperature never reaches the sprayed material melting temperature. This suggests that CS coatings are produced solely as a result of intense local plastic deformation (Ref 7-10), although some researchers have shown that local melting is theoretically possible (Ref 11). Consequently, CS is referred to in the literature as a solid-state process.

Given the absence of significant heating and its resulting grain-growth mechanism and chemical changes, the CS process has shown a significant potential for the production of coatings having a microstructure as well as mechanical and chemical properties similar to that of the original feedstock particles. As such, it has been used to produce nanocrystalline coatings from nanocrystalline feedstock (Ref 12-16). Consequently, and as shown in this work, CS can possibly be used to produce amorphous coatings from an amorphous gas-atomized feedstock powder.

There has been an increasing interest in producing iron-base amorphous alloy coatings because of their attractive combinations of engineering properties: high strength and hardness, improved wear resistance, and superior corrosion resistance (Ref 17-19). In addition, the nanostructure in metallic coatings can be developed by postprocessing the metallic amorphous coating through a solid-state transformation (Ref 20). However, the formation of an amorphous alloy structure is quite difficult and requires high cooling rates, normally above 10^5 K/s to prevent detectable crystallization (Ref 21). Recent interest in amorphous iron (Fe) stems from the observation that certain compositions will retain an amorphous microstructure, even under relatively low cooling rates (Ref 20).

In the past decade, a series of new bulk amorphous alloys with a multicomponent chemistry and high glass forming ability (GFA) have been developed in zirconium-, magnesium-, lanthanum-, palladium-, titanium-, and Fe-base systems with various rapid solidification techniques (Ref 21-26). The discovery of bulk amorphous alloys has opened up bright prospects for the synthesis of thick amorphous alloy coatings.

Compared with other amorphous alloy systems, such as zirconium- and lead-base metallic glasses, the advantages of Fe-base amorphous coatings are lower materials cost, higher strength, and higher wear and corrosion resistance. The major obstacle to Fe-base amorphous alloy production is their limited GFA (Ref 17). It was reported that the addition of molybdenum (Mo) increases the amorphous forming ability of carbon iron alloys (Ref 27, 28), while the addition of Mo and tungsten (W) to Fe-base alloy enhances the corrosion resistance of the amorphous alloys (Ref 29-31).

To explore the possibility of producing amorphous feedstock powder from gas atomization that is suitable for thermal spray processes, an exploratory study on the multicomponent Fe-base alloy (Fe-Cr-Mo-W-C-Mn-Si-Zr-B) coating production by CS was carried out in the present work. The novel Fe-base amorphous coating produced is believed to have a considerable po-

This article was originally published in *Building on 100 Years of Success, Proceedings of the 2006 International Thermal Spray Conference* (Seattle, WA), May 15-18, 2006, B.R. Marple, M.M. Hyland, Y.-Ch. Lau, R.S. Lima, and J. Voyer, Ed., ASM International, Materials Park, OH, 2006.

L. Ajdelsztajn, and **E.J. Lavernia,** Dept. of Chemical Engineering and Materials Science, University of California, Davis; and **B. Jodoin, P. Richer** and **E. Sansoucy,** Dept. of Mechanical Engineering, University of Ottawa, Ottawa, Canada. Contact e-mail: jodoin@genie.uottawa.ca.

tential for advanced engineering applications due to their advantageous properties and limitless coating thickness since the critical cooling rate is not an issue in the CS coating process.

2. Experimental Procedures

Iron-base (Fe-Cr-Mo-W-C-Mn-Si-Zr-B) feedstock powder was prepared by gas-atomization (SHS727 powder, The NanoSteel Company, Maitland, FL). The gas-atomized powder was sieved using a 400-mesh sieve and sprayed onto grit-blasted Al-6061 substrates using the CS coating system developed at the University of Ottawa Cold Spray Laboratory. This system has been used extensively to spray a variety of coatings (Ref 12-16). It consists of a computer-controlled gas system, a commercial Praxair 1264 powder feeder (Indianapolis, IN), a spray gun, and a sealed-off spraying chamber, providing the possibility of recycling the powder that has not adhered to the substrate. The spray gun, a converging-diverging nozzle, allows the gas to reach the supersonic velocities required by the process. Pressure and temperature probes are incorporated throughout the system to monitor the process parameters and stability. The nozzle inlet pressure and temperature were respectively set at 1 MPa and 300 °C. The substrate holder is equipped with a one-axis travel displacement system. The coating was obtained by moving the substrate at a constant velocity in front of the jet exiting the spraying gun. The spraying standoff distance used was 20 mm, and a single passage of the substrate in front of the gun was used to build up the coating on the substrate. A single passage was used to minimize the processing time.

Particle velocities were measured with a laser in-flight diagnostic system, a DPV-CPS (Tecnar Automation Ltd., St-Bruno, Québec, Canada). While a continuous laser illuminates a measurement volume, a dual-slit photomask captures the signal generated by individual particles passing in front of the sensor. The signal from the photosensor is amplified, filtered, and analyzed. In-flight diagnostic of each individual particle that crosses the measurement volume is performed by determining the time between the two peaks of the particle signal. Particle velocities are then obtained by dividing the distance between the two slits by their time of flight. In this study, the velocity measurements were taken at a point 5 mm from the spraying gun exit.

Microstructural analysis of the gas-atomized feedstock powder and coatings was conducted using scanning electron microscopy (SEM). X-ray diffraction (XRD) measurements were carried out with a Scintag (Cupertino, CA) XDS-2000 diffractometer equipped with a graphite monochromator using Cu Kα radiation at 100 steps per degree and a count time of 5 s per step. To investigate the mechanical properties of the coatings, nanoindentation studies were conducted using a MTS (Oak Ridge, TN) Nanoindenter XP (Berkovich indenter) on the cross section of the sprayed coatings. Samples were prepared for nanoindentation by mixing the coatings with a conductive molding compound. The samples were then ground (1200 grit) and polished (6, 3, 1, 0.25 μm diamond slurry). The continuous stiffness measurement (CSM) approach was used to determine the hardness values from the nanoindentation tests (Ref 32). An indentation depth of 500 nm was chosen in this study. Vickers microhardness tests were also performed on the cross section of the coatings using a load of 300 gf and a dwell time of 15 s with a Buehler (Lake Bluff, IL) Micromet 2004 indenter. The reported values are the average of 15 indentations for each sample.

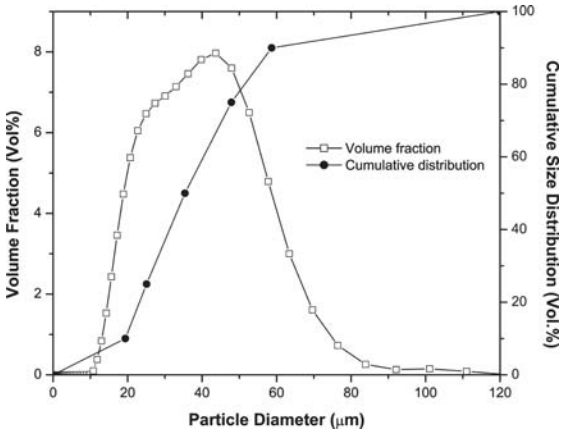

Fig. 1 Size distribution of the as-received Fe-base alloy powder

3. Results and Discussion

3.1 Powder Characterization

The size distribution of the as-received Fe-base alloyed powder produced by gas atomization is presented in Fig. 1 in a log normal distribution as well as the cumulative size distribution.

It has been shown that the cooling rate or glass formation is a strong function of the particle size (Ref 19). Consequently, it is desired to produce a high fraction of fine powder particles from the gas-atomization process. Figure 1 shows that the powder particles with a diameter smaller than 38 μm constitute about 50% of the total volume.

Direct SEM observations of the atomized powder particles show that most of the particles exhibit a spherical morphology (Fig. 2a). The backscattered electron (BSE) image of the cross section of the powder is shown in Fig. 2(b). In general, one can observe, with few exceptions, that the powder particles under 20 μm in diameter show an undistinguished microstructure, indicating that no crystallization has occurred. However, primary crystallization from the supercooling liquid occurred during solidification and is observable in larger particles. As the powder size increases, the microstructure becomes coarser and new crystalline phases precipitate. This supports observations that the cooling rate in gas atomization increases with decreasing of the powder size. Featureless particles can be generally considered fully amorphous, although an exhaustive determination typically requires transmission electron microscopy analysis. The SEM observations suggest that the large particles are partially amorphous with XRD measurements revealing primary crystalline αFe while other precipitations appear in the amorphous matrix.

The formation of metallic amorphous powders produced by gas atomization depends on the alloy composition and the atomization conditions. The present Fe-base alloy has a high GFA (Ref 25). The mechanism for the large GFA can be interpreted in structural, thermodynamic, and kinetic aspects. The base com-

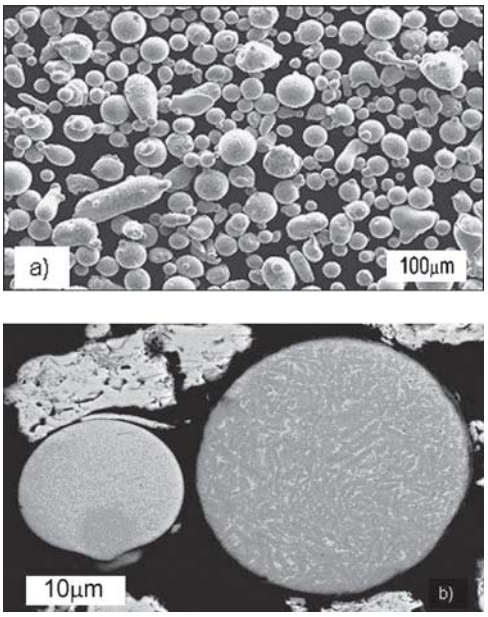

Fig. 2 SEM images showing (a) the morphology and (b) the cross section of the atomized Fe-base alloy powder

position in the present alloy is the Fe-Mn-Cr-B system (Ref 21), which satisfies the three empirical rules proposed by Inoue et al. (Ref 25): multicomponent alloy systems consisting of more than three constituent elements, significantly different atomic size ratios above approximately 13%, and suitable negative heats of mixing among the constituent elements. The effective addition of Mo, W, zirconium (Zr), carbon (C), and silicon (Si) causes the sequential change in the atomic size, as well as the generation of new atomic pairs with various negative heats of mixing. The highly dense random packed structure was formed with low atomic diffusivity in the supercooled liquid caused by the topological and chemical short-range order (Ref 33). The structural studies indicated that the highly dense, randomly packed structure of the amorphous alloy results from large atomic size ratios in the multicomponent system (Ref 22, 25). The nucleation and growth of the crystalline phase can be suppressed in the supercooled liquid by inhibiting the long-distance diffusion and increasing the melting viscosity. The structural features of the Fe-base alloy make the nucleation and growth of crystalline phases from the initially homogeneous supercooled liquid extremely difficult, due to the extremely slow mobility of the constituents in the high viscous supercooled liquid. It becomes difficult for the nine elements of the alloy to simultaneously satisfy the composition and structural requirements of the crystalline compounds. Therefore, the fine powder (higher cooling rates) enables the formation of featureless amorphous powder. The same is not true for the large particles where, even with a high GFA, alloy precipitation of crystalline phases is still possible during gas atomization.

Figure 3 presents the measured particle velocity distribution during spraying, using the specified operating parameters. The particle velocities range between 450 and 1000 m/s, with an average of 706 ± 105 m/s. The deposition efficiency was evaluated at 85%, under the specified operating parameters. Examination of Fig. 3 reveals that more than 86% of the particles were accelerated above 600 m/s, suggesting a critical velocity close to 600 m/s for this Fe-base alloy.

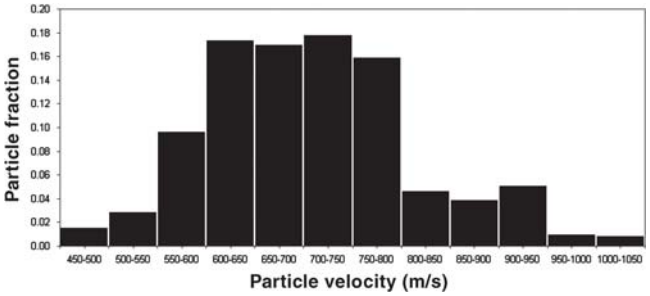

Fig. 3 Measured particle velocity distribution during deposition

A validated numerical model developed for the CS process was used to assess the effect of the particle size distribution on the velocity distribution measured in this study. The model predicts the aerodynamic fields of the CS process by solving the Reynolds-Averaged Navier-Stokes (RANS) equations with the proper boundary conditions. The injected particles position and velocity histories are predicted by solving Newton's law of motion using an Eulerian-Lagrangian approach. More details on the model and its validation can be found elsewhere (Ref 34). Table 1 presents the comparison of particle velocities 5 mm from the exit of the spray gun used in this work as predicted by the numerical model for typical particle size found in the sieved feedstock powder.

It was found that the range of particle velocities predicted by the numerical model matches the range of particle velocities measured experimentally. Furthermore, the model results revealed that the smallest particles are the ones reaching the highest exit velocity; above 1000 m/s and that the largest particles were the ones exiting the spray gun at the lower end of the velocity range. Finally, the average velocity measured (706 m/s) matches the velocity range of the average size particles predicted by the model (657 to 800 m/s). The deviation between the experimental and model results are attributed to the particle energy losses that are not considered in the model as experienced in interparticle and wall-particle collisions.

3.2 Coating Characterization

Figure 4 shows a secondary electron image of a coating produced by CS with the gas-atomized powders. Limited or no porosity is present in the coating, and no microcracks or defects can be observed between particles, despite the high deposition rate used (approximately 250 μm for a single passage of the gun). The lack of defects and porosity at the particle/particle and particle/substrate interfaces suggests an adequate particle kinetic energy during deposition that was able to generate particle velocities above the alloy critical velocity and thus creating an intimate bonding at the interfaces (particle/particle and particle/substrate).

It is also observed that the top surface of the coating is free of cracks and porosity as opposed to previously reported CS coating microstructures in aluminum, nickel, and titanium alloys (Ref 4, 5, 15). In these studies, the presence of cracks and porosity at the top layer of the coating was attributed to the fact that

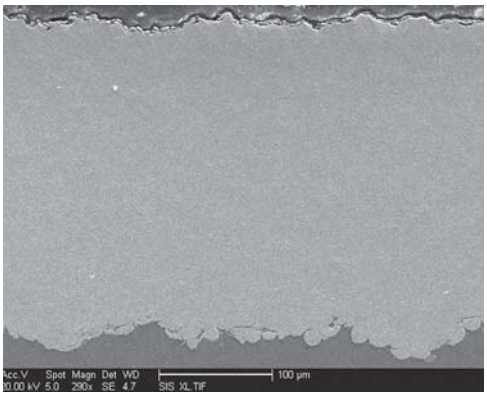

Fig. 4 SEM cross-section of the coating produced with the atomized Fe-base alloy powder

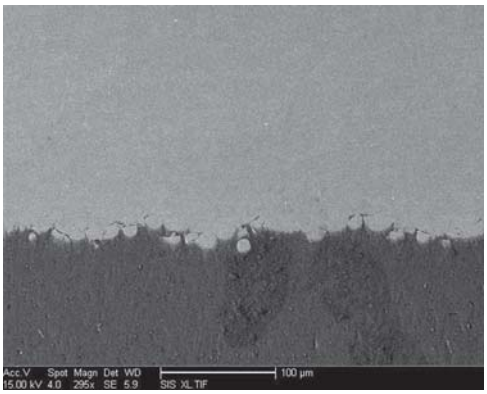

Fig. 5 Secondary electron image of the interface between the cold sprayed coating and the aluminum substrate

Table 1 Predicted particle velocities for different sizes 5 mm from the exit of the spray gun

Powder particle size, μm	10	20	30	40	50
Particle exit velocity, m/s	1090	800	657	571	513

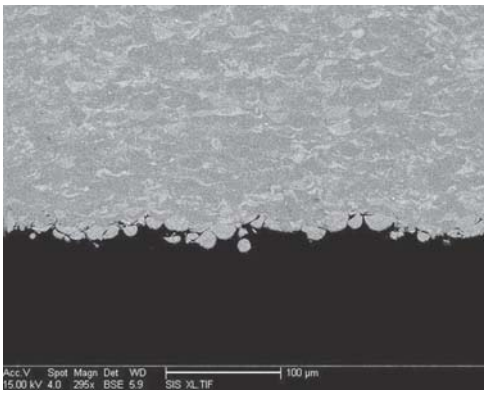

Fig. 6 Backscattered electron image of Fig. 5. Light gray corresponds to crystalline regions and dark gray corresponds to fully amorphous regions.

for these materials, tamping of the deposited layers is required to achieve dense coating and this tamping mechanism cannot occur in the top layer. However, in the current study, the results suggest that the densification of the coating was achieved without the tamping effect. One can speculate that the particle impact velocity was high enough to promote the adiabatic regimen created during the impact. That can lead to thermal softening by raising the temperature of the particles to values near the glass transition temperature (T_g = 468 °C) of the amorphous alloys. This would facilitate the plastic deformation and mechanical interlocking of splats, each particle conformably shaping to the previous layer producing a dense coating, and the localized adiabatic shear instability at the particles boundaries helping the creation of intimate contact between clean surfaces promoting metallurgical bonding at the particle/particle surfaces and making it possible to achieve very high densities in the coating.

Figures 5 and 6 show secondary and backscattered images of the coating and the coating/substrate interface. The presence of precipitates throughout the coating microstructure suggests that, as with the gas-atomized powder, not all the particles were completely amorphous. This also indicates that no microstructural changes are observed in the coating microstructure when compared with the feedstock powder, where one can find amorphous and crystalline phases depending on the particle size (cooling rate dependent during solidification in the atomization step). Figure 7 shows the XRD patterns for the powder and the cold sprayed coating. The results corroborate the fact that no microstructural changes are observed in the material before and after spray.

Figure 8 shows a high magnification of Fig. 6 where crystalline phases (bright phases) and amorphous regions (darker areas) are observed. Furthermore, undeformed spherical particles embedded deep into the substrate are also observed. This could be explained by the fact that the initial sprayed particles hit the soft substrate. This provides a relatively soft impact to the hard impinging particles, leading to an extensive substrate deformation and very limited particle deformation (hardness reported in Table 2). The successive impact of hard particles depositing at the surface eventually forms a hard layer where the rest of the particles can severely deform upon impact due to their compatible hardness values and form a dense coating.

3.3 Hardness Analysis

Figure 9 presents a microhardness Vickers indentation mark (300 g) and some shear deformation on the edges of the indentation mark as seen in bulk amorphous materials. It is also observed that no interparticle cracks can be seen after the indentation, which is an important indication of the coating integrity (strong particle/particle bonding). The microhardness value of the coating is 639 ± 16 HV_{300g}.

To explain the mechanical response of the amorphous and crystalline material that constitutes the coating, nanoindentation measurements were performed on splats of the sprayed coatings. The results are summarized in Table 2, where one can note that the powders with crystalline phases are approximately 1.5 times harder than the fully amorphous ones and approximately 12 times harder than the substrate.

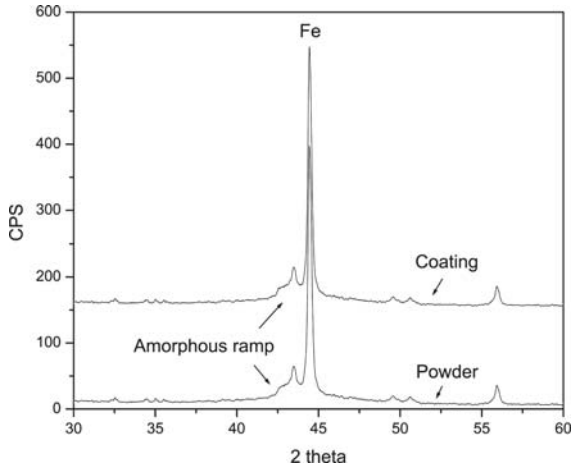

Fig. 7 XRD patterns for the powder and the coating

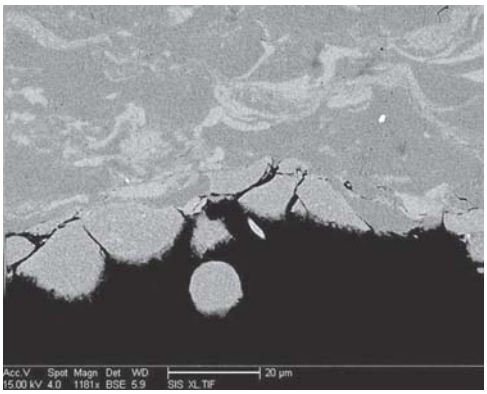

Fig. 8 Higher magnification of the SEM image shown in Fig. 6. A spherical powder particle is embedded deep into the aluminum substrate (no sign of extensive plastic deformation).

Table 2 Nanoindentation results for the crystalline and amorphous splats

Nanoindentation	Hardness, GPa	Elastic modulus, GPa
Crystalline splats	15.2 ± 0.2	278 ± 25
Amorphous splats	10.4 ± 0.6	260 ± 9
Aluminum substrate	1.2 ± 0.1	74 ± 6

The nanoindentation results corroborate the observed phenomenon (Fig. 8) where the very hard particles penetrate the substrate without deforming themselves, and once a first layer is formed the subsequent particle impacts have higher hardness compatibility, allowing the severe deformation of both the impacted and impacting particles.

4. Conclusions

Cold sprayed Fe-base amorphous alloy coatings were successfully produced. The coatings showed a negligible porosity and excellent interfaces with the substrate material. The microstructure of the feedstock powder (gas atomized) was retained after the spray process, fine particles (completely amorphous) remained amorphous after the impact, and the larger and crystallized particles also retained their initial microstructure.

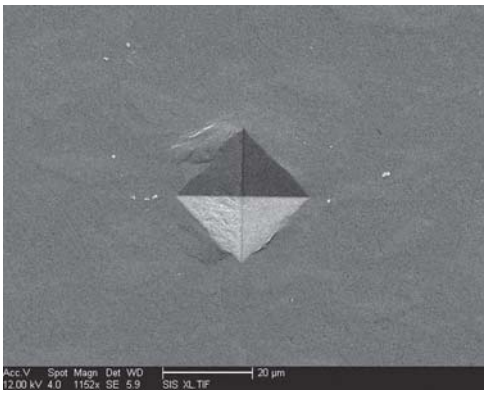

Fig. 9 Vickers indentation (300 g) on the amorphous coating (no signs of interparticle crack propagation)

It is believed that the localized adiabatic shear instability at the particles boundaries helps the creation of intimate contact between clean surfaces that result in a metallurgical bonding at the particle/particle surfaces. One can speculate that the adiabatic regimen created during the impact could raise particle temperatures close to the glass transition temperature (T_g) of the amorphous alloys, leading to particle softening and making it possible to achieve very high densities in the coating.

It is proposed that for the soft substrates and hard particles used in this work, the first impacts will primarily confine the deformation to the substrate material, and after the first layer of undeformed hard particles are created the subsequent impacts provide severe plastic deformation on both substrate and impacting particles.

References

1. C. Li and W. Li, Impact Fusion Phenomenon During Cold Spraying of Zinc, *Thermal Spray 2004: Advances in Technology and Application,* May 10-12, 2004 (Osaka, Japan), ASM International, 2004, 1129 pages
2. C. Borchers, F. Gärtner, T. Stoltenhoff, H. Assadi, and H. Kreye, Microstructural and Macroscopic Properties of Cold Sprayed Copper Coatings, *J. Appl. Phys.,* 2003, **93,** p 10064-10070
3. R. Morgan, P. Fox, R. Morgan, P. Fox, J. Pattison, C. Sutcliffe, and W. O'Neill, Analysis of Cold Gas Dynamically Sprayed Aluminum Deposits, *Mater. Lett.,* 2004, **58,** p 1317-1320
4. C.-J. Li and W.-Y. Li, Deposition Characteristics of Titanium Coating in Cold Spraying, *Surf. Coat. Technol.,* 2003, **167**(2-3), p 278-283
5. T.H. Van Steenkiste, J.R. Smith, and R.E. Teets, Aluminum Coatings via Kinetic Spray with Relatively Large Powder Particles, *Surf. Coat. Technol.,* 2002, **154**(2-3), p 237-252
6. R.S. Lima, J. Karthikeyan, C.M. Kay, J. Lindemann, and C.C. Berndt, Microstructural Characteristics of Cold-Sprayed Nanostructured WC-Co Coatings, *Thin Solid Films,* 2002, **416**(1-2), p 129-135
7. R.C. Dykhuizen, M.F. Smith, D.L. Gilmore, R.A. Neiser, X. Jiang, and S. Sampath, Impact of High Velocity Cold Spray Particles, *J. Thermal Spray Technol.,* 1999, **8**(4), p 559-564
8. H. Assadi, F. Gärtner, T. Stoltenhoff, and H. Kreye, Bonding Mechanism in Cold Gas Spraying, *Acta Mater.,* 2003, **51,** p 4379-4394
9. A.P. Alkhimov, A.I. Gudilov, V.F. Kosarev, and N.I. Nesterovich, Specific Features of Microparticle Deformation upon Impact on a Rigid Barrier, *J. Appl. Mech. Tech. Phys.,* 2000, **41,** p 188-192

10. M. Grujicic, J.R. Saylor, M. Grujicic, J.R. Saylor, D.E. Beasley, W.S. DeRosset, and D. Helfritch, Computational Analysis of the Interfacial Bonding Between Feed-Powder Particles and the Substrate in the Cold-Gas Dynamic-Spray Process, *Appl. Surf. Sci.,* 2003, **219**(3-4) p 211-227
11. T. Schmidt, F. Gärtner, T. Schmidt, F. Gärtner, H. Assadi, T. Stoltenhoff, and H. Kreye, High Velocity Impact Phenomena and Coating Quality in Cold Spraying, *Thermal Spray 2005,* May 2-4, 2005 (Basel, Switzerland), ASM International, 2005, p 232-238
12. L. Ajdelsztajn, B. Jodoin, G.E. Kim, J. Schoenung, L. Ajdelsztajn, B. Jodoin, G.E. Kim, and J.M. Schoenung, Cold Spray Deposition of Nanocrystalline Aluminum Alloys, *Met. Mater. Trans. A,* 2005, **36,** p 657-666
13. P. Richer, B. Jodoin, and L. Ajdelsztajn, Characteristics of Cold Sprayed Coatings Using Nano-Aluminum and Nano-Nickel Powders, 16th Canadian Materials Science Conference (Ottawa, Ontario, Canada), June 2004
14. E. Sansoucy, B. Jodoin, and L. Ajdelsztajn, Conventional and Nano-Structured Nickel Coatings Produced by Cold Spray Processing, 16th Canadian Materials Science Conference (Ottawa, Ontario, Canada), June 2004
15. L. Ajdelsztajn, B. Jodoin, and J. Schoenung, Synthesis and Mechanical Properties of Nanocrystalline Ni Coatings Produced by Cold Gas Dynamic Spray, *Surf. Coat. Technol.,* 2006, 201(3-4), p 1166-1172
16. L. Ajdelsztajn, A. Zuniga, B. Jodoin and E. Lavernia, Cold Gas Dynamic Spraying of a High Temperature Al Alloy, *Surf. Coat. Technol.,* in press. Corrected proof, Available online 19 July 2005
17. Z.P. Lu, C.T. Liu, J.R. Thompson, and W.D. Porter, Structural Amorphous Steels, *Phys. Rev. Lett.,* 2004, **92,** p 245503
18. S.J. Pang, T. Zhang, K. Asami, and A. Inoue, Synthesis of Fe-Cr-Mo-C-B-P Bulk Metallic Glasses with High Corrosion Resistance, *Acta Mater.,* 2002, **50,** p 489-497
19. W.L. Johnson, Bulk Amorphous Metal—An Emerging Engineering Material, *JOM,* 2002, **54**(3), p 40-43
20. D.J. Branagan, W.D. Swank, D.C. Haggard, and J.R. Fincke, Wear-Resistant Amorphous and Nanocomposite Steel Coatings, *Met. Mater. Trans.,* 2001, **32A,** p 2615-2621
21. A.V. Sergueeva, N.A. Mara, J.D. Kuntz, D.J. Branagan, and A.K. Mukherjee, Shear Band Formation and Ductility of Metallic Glasses, *Mater. Sci. Eng. A,* 2004, **383**(2), p 219-223
22. W.L. Johnson, Fundamental Aspects of Bulk Metallic Glass Formation in Multicomponent Alloys, *Mater. Sci. Forum,* 1996, **35,** p 225-227
23. R. Busch, Y.J. Kim, and W.L. John, Thermodynamics and Kinetics of the Undercooled Liquid and the Glass-Transition of the Zr41.2Ti13.8Cu12.5Ni10.0Be22.5 Alloy, *J. Appl. Phys.,* 1995, **77,** p 4039-4043
24. A. Peker and W.L. Johnson, A Highly Processable Metallic-Glass—Zr41.2Ti13.8Cu12.5Ni10.0Be22.5, *Appl. Phys. Lett.,* 1993, **63,** p 2342-2344
25. A. Inoue, Thermal Properties of Zr-TM-B and Zr-TM-Ga (TM = Co, Ni, Cu) Amorphous Alloys with Wide Range of Supercooling, *Mater. Trans. JIM,* 1995, **36,** p 1411-1419
26. A. Inoue, T. Zhang, and T. Masumoto, Aluminum-Base Amorphous Powders with Flaky Morphology Prepared by a 2-Stage Quenching Technique, *Mater. Trans. JIM,* 1989, **30,** p 1033-1043
27. K. Kishitake, H. Era, and P. Li, Nonequilibrium Phases In Rapidly Solidified High-Carbon Fe-Cr-Mo Alloys, *Mater. Trans. JIM,* 1993, **34,** p 54-61
28. A. Inoue, T. Masumoto, S. Arakawa, and T. Iwadachi, Amorphous High-Carbon Alloy-Steels Rapidly Quenched from Melts, *Trans. JIM,* 1978, **19,** p 303-304
29. H. Habazaki, A. Kawashima, K. Asami, and K. Hashimoto, The Effect of Tungsten on the Corrosion Behavior of Amorphous Fe-Cr-W-P-C Alloys in 1m HCl, *J. Electrochem. Soc.,* 1991, **138,** p 76-81
30. K. Kobayashi, K. Hashimoto, and T. Masumoto, Spontaneously Passivating Amorphous Fe-Cr-Mo-Metalloid Alloys in 6 NHCl at Room-Temperature and 80-Degrees-C, *Sci. Rep. Res. Inst. Tohoku Univ. [Med],* 1981, **A29,** p 284-295
31. H. Habazaki, A. Kawashima, K. Asami, and K. Hashimoto, The Corrosion Behavior of Amorphous Fe-Cr-Mo-P-C and Fe-Cr-W-P-C Alloys in 6-M HCl Solution, *Corros. Sci.,* 1992, **33,** p 225-236
32. X. Li and B. Bhushan, A Review of Nanoindentation Continuous Stiffness Measurement Technique and Its Applications, *Mater. Charact.,* 2002, **48,** p 11-36
33. A. Mitra; H.-Y. Kim, D.V. Louzguine, N. Nishiyama, B. Shen, and A. Inoue, Magnetic Properties of Melt-Spun and Annealed Fe62Co9.5Gd3.5Si10B15 Alloy, *J. Phys. D, Appl. Phys.,* 2003, 36(18), p 2234-2238
34. B. Jodoin, F. Raletz, and M. Vardelle, Cold Spray Modeling and Validation Using an Optical Diagnostic Method, *Surf. Coat. Technol.,* 2006, **200,** p 4424-4432